Title: Metal-support interaction in catalysis: the influence of the morphology of a nano-oxide domain on catalytic activity

Authors: Sharif Najafishirtari, Clara Guglieri, Sergio Marras, Alice Scarpellini, Rosaria Brescia, Mirko Prato, Giulia Righi, Anna Franchini, Rita Magri, Liberato Manna, Massimo Colombo

PII: S0926-3373(18)30567-8
DOI: https://doi.org/10.1016/j.apcatb.2018.06.033
Reference: APCATB 16781

To appear in: *Applied Catalysis B: Environmental*

Received date: 19-4-2018
Revised date: 1-6-2018
Accepted date: 11-6-2018

Please cite this article as: Najafishirtari S, Guglieri C, Marras S, Scarpellini A, Brescia R, Prato M, Righi G, Franchini A, Magri R, Manna L, Colombo M, Metal-support interaction in catalysis: the influence of the morphology of a nano-oxide domain on catalytic activity, *Applied Catalysis B: Environmental* (2018), https://doi.org/10.1016/j.apcatb.2018.06.033

Metal-support interaction in catalysis: the influence of the morphology of a nano-oxide domain on catalytic activity

Sharif Najafishirtari[a], Clara Guglieri[b], Sergio Marras[c], Alice Scarpellini[d], Rosaria Brescia[d], Mirko Prato[c], Giulia Righi[e], Anna Franchini[e], Rita Magri[e], Liberato Manna[a], Massimo Colombo[a]*

[a] Nanochemistry Department, Istituto Italiano di Tecnologia, Genoa, 16163, Italy

[b] Sincrotrone Trieste, ELETTRA, 34012 Basovizza (TS), Italy

[c] Materials Characterization Facility, Istituto Italiano di Tecnologia, Genoa, 16163, Italy

[d] Electron Microscopy Facility, Istituto Italiano di Tecnologia, Genoa, 16163, Italy

[e] Dipartimento di Scienze Fisiche, Informatiche e Matematiche (FIM), Università degli Studi di Modena e Reggio Emilia, 41125 Modena, Italy

**Corresponding author: massimo.colombo@iit.it*

Graphical Abstract

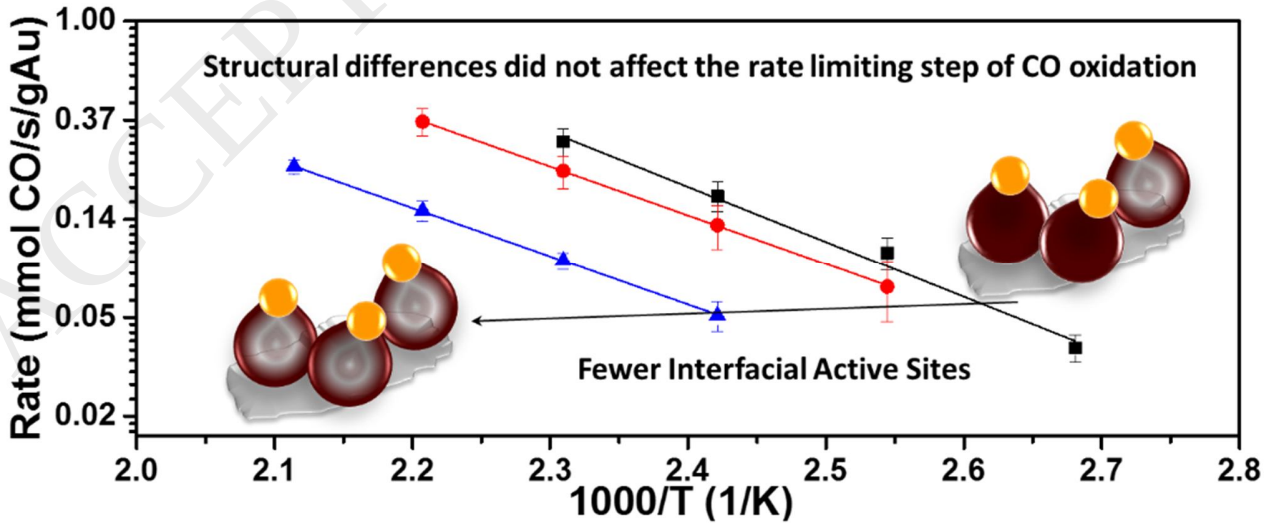

Highlights

- How hollow oxide morphology affects the CO oxidation of supported Au NPs
- Hollow oxide morphology affected the surface charge of Au domain
- Hollow oxide morphology affected reducibility and crystallinity of oxide domain
- Structural differences did not affect the rate limiting step of CO oxidation
- Hollow oxide morphology affected the number of active sites

Abstract:

Using wet chemistry synthesis methods we prepared nanodumbbell structures as a model oxide supported metal catalyst. In this peculiar configuration, a single metallic domain (M) is connected to a single metal oxide (MOx) one. The size, composition and morphology of each domain can be carefully controlled, allowing us to investigate the effects resulting from a hollow morphology of the MOx domains, while all other material's properties were kept constant. We chose the CO oxidation as a model oxidation reaction and increasing the population of nanocrystals (NCs) with hollow oxide domains resulted in a decrease in catalytic activity. Despite the manipulation of oxide morphology affected the surface charge of the Au domain, the bulk oxide reducibility and the crystallinity of the nanosized oxide support, the rate limiting step of CO oxidation was not affected. The same apparent activation energy was indeed measured independently from the population of NCs with hollow oxide domains. The difference in catalytic performance was thus ascribed to a different number of interfacial active sites when the morphology evolved from full to hollow.

Keywords:

metal-oxide catalysts; gold; nanodumbbells, Metal-support interaction, oxidation catalysis

1. Introduction

It is established in the literature that the metal-support interaction (MSI) is a key factor in defining the activity of metal supported catalysts [1-7], a family of heterogeneous catalysts that is widely employed in environmental catalysis[8,9]. In addition, MSI can also be responsible for the stability of

the catalysts through preventing or facilitating sintering [10]. Indeed, the metal-support boundary sites can be largely responsible for the promotion of individual reaction steps that can subsequently enhance the overall catalytic activity [1,7,11,12]. There are different mechanisms such as charge transfer, spill over and perimeter activation which can describe how the MSI can enhance the catalytic properties [13]. Nevertheless, two aspects of the interface can be considered fundamentally important, namely the electronic properties which cause the charge transfer, and the chemical interaction either in the form of an atom transfer [2] or stabilization of low-coordinated atoms [14]. Several works have been published which study the significance of MSI and how to manipulate it. For example, Bruix et al. have identified a new type of strong MSI in a single crystal model catalyst of Pt/CeO_2 which produces a large electronic perturbation for small Pt particles in contact with ceria and, subsequently, is responsible for its enhanced activity in the water gas shift reaction [15]. Regarding the effect of synthesis methods on MSI for a Pt/NCNT catalytic system, Ning et al. have reported how different synthesis conditions and subsequent changes in electronic properties correlate with different activities [6]. Cargnello et al. studied the role of MSI in CO oxidation, using pre-made Pd, Ni and Pt with different sizes on ceria and alumina. They concluded that the size dependent activities indeed arose from the different number of interfacial atoms at the perimeter of the metals in contact with the supports [12]. In contrast, Yu et al. have reported that the strong MSI for Au/TiO_2 has a major influence on the electronic structure of the Au, dominating the effect of size reduction [14]. These results indicate that it is still important to isolate the significance of different structural parameters, including MSI, and to understand how they affect the activity [13,16], particularly when dealing with nanomorphology-induced catalytic properties [17]. This is hardly ever achieved by studying the catalyst prepared by conventional methods, simply because obtaining a uniform set of active species could be quite difficult and challenging. Colloidal synthesis approaches, on the other hand, provide the tools to prepare the targeted materials with well-defined structural properties. Such materials can then be used to gain fundamental understanding of the catalytic functions [18]. Among different types of colloidal nanocrystals (NCs), those with a dumbbell-like morphology represent a very important class of materials that is characterized by a nanosized metal (M) and a metal oxide (MOx) domain which are epitaxially attached to each other [19-21]. They provide an ideal system for fundamental studies regarding the influence of different parameters, such as metal size or composition and metal-support interaction, in a catalytic system. For example, we have previously shown that the CO oxidation activity at constant Au loading is essentially related to the interface between Au and iron oxide, which is promoted by decreasing the Au domain size at a similar Au surface charge and at the same nanosized support [22]. In another work, we showed the superior

thermal stability of the metallic NPs when attached to a nanosized support, which resulted in a significant improvement in the activity compared to bulk-supported NPs [20].

In this work, we have studied how the morphology of the nanosized oxide support in a nanodumbbell structure influences the stability of the metal domain, the MSI and the catalytic activity in CO oxidation. Specifically, we investigated the effects resulting from a hollow morphology of the MOx domains. Different catalyst batches were prepared, consisting of dumbbell-like NCs having the same size of the M domains and the same external diameter for the MOx ones, while the population of the NCs with a hollow oxide domain was different among the batches (as schematically shown in Scheme 1). The prepared materials were used as catalysts in the CO oxidation reaction and were extensively characterized in order to establish the structure-activity correlation for the selected reaction. Indeed, we observed a difference in activity among the samples i.e. the catalyst with a higher population of hollow oxide NCs was less active. They had the same sizes of M and MOx domains but where characterized by (i) different surface charge of the Au domains; (ii) different reducibility of the MOx domain; (iii) increase disorder in the MOx and the appearance of a minor fraction of hematite phase as the population of hollow MOx domains increased. Yet, the same apparent activation energy was measured for all the samples. This experimental evidence indicates that none of these changes was found to significantly affect the rate limiting step of the CO oxidation reaction, likely the abstraction of O from the interfacial metal/metal oxide sites [7]. The lower activity in case of hollow particles was thus attributed to a lower number of interfacial active sites.

2. Experimental

2.1. Chemicals

Oleylamine (OlAm, 70%), $HAuCl_4 \cdot 3H_2O$, 1-octadecene (ODE, Technical grade 90%), oleic acid (OlAc, technical grade 90%), iron pentacarbonyl (>99.99% trace metals basis), solvents (ethanol, isopropanol, toluene and n-hexane) were purchased from Sigma Aldrich. The γ-Al_2O_3 extrudate (SSA = 220 m^2/g; average pore diameter = 6.5 nm) was purchased from Strem Chemicals and silica (crystalline fine, coating quality, ≥99.9%) was obtained from Sigma Aldrich. All chemicals were used as received without further purifications.

2.2. Synthesis of AuCu- Iron Oxide (AuCu/FeOx) NCs

AuCu/FeOx NCs were typically synthesized by a seed-mediated growth approach [20], using pre-made AuCu NCs, synthesized based on the protocols described in [23], and iron pentacarbonyl was used as the iron source. Typically, a specific volume of AuCu colloidal solution corresponding to 8 mg of the AuCu was mixed with 20 ml of ODE, 3 ml of OlAm, 1.0 ml of OlAc. Other batches were synthesized using lower volumes of OlAc (i.e. 0.5 and 0.2 ml) to induce less oxidation of the Fe in the oxide domain and to manipulate the population of dumbbells with an Fe-rich core in the oxide domain. The mixture was then degassed under vacuum at 80 °C for 1 h to remove hexane i.e. the solvent dispersing the AuCu NCs. Then, the atmosphere was switched to N_2 and the temperature was raised to 205 °C. Meanwhile, a solution of 80 µl Fe precursor in 1 ml of already-degassed ODE was injected into the solution at 150 °C. The mixture was stirred for 1.5 h and then it was heated up to 300 °C and kept there for 1 h. The products were washed twice with a mixture of isopropanol and ethanol (3:1 vol. ratio), then centrifuged and dispersed in 10 ml of toluene. The samples were tagged as D1, D2 and D3, corresponding to the NCs synthesized using 1.0, 0.5 and 0.2 ml of OlAc, respectively. The synthetic procedure, along with the main controlling parameters, is illustrated in Scheme 2.

2.3. Catalyst Preparation

The alumina supported catalysts were prepared by a colloidal deposition of as-prepared dumbbell NCs. Typically, a specific weight of γ-Al_2O_3 powder (manually crushed and sieved to 90 µm) was dispersed in toluene then a proper amount of colloidal solution (targeting 1.0 wt.% Au) was added to it and the suspension was sonicated for 2 h. After deposition, the transparent supernatants were removed and the catalysts were dried in an air atmosphere at 80 °C for 3 h. The catalysts were also subsequently calcined in static air for 10 h at 350 °C to remove the protecting ligands from the surface of the NCs [20]. The samples were labeled as D1-A, D2-A and D3-A, corresponding to the activated catalysts that were prepared from NCs using 1.0, 0.5 and 0.2 ml of OlAc in their syntheses, respectively.

2.4. Activity Measurements

The activity of the catalysts for CO oxidation in the kinetic regime was measured using a micro-reactor system coupled with a micro-Gas Chromatographer (µ-GC) equipped with three modules working in parallel (each consisting of an injector, a column and a thermal conductivity detector) to analyze the CO, O_2 and CO_2 (SRA Instruments model R-3000). The catalyst powder was diluted with silica powder (manually crushed and sieved to 90 µm, 1:9 weight ratio), loaded into the reactor, pre-treated at 350 °C for 10 h (heat rate 5 °C/min), and finally cooled down to room temperature in an

oxidizing atmosphere of 6% v/v O_2 balanced with He. Next, the feed gas was introduced into the reactor and the temperature was raised stepwise. Each temperature was maintained for 2 h to reach the steady state conditions. The feed gas was a mixture of 1% v/v CO and 6% v/v O_2 balanced with He with a flow rate of 80 Ncc/min, corresponding to a weight hourly space velocity (WHSV) of 24'000'000 Ncc/h/(g Au). Kinetic measurements were repeated twice for the same loaded batch, and at least twice using different aliquots of the same catalyst, in order to verify the reproducibility and the precision of the data. Experimental conditions were selected in order to keep the CO conversion below 15% and work under differential conditions.

2.5. Characterization

2.5.1. Transmission Electron Microscopy (TEM)

Overview bright-field (BF) TEM images were acquired using a JEOL JEM-1011 instrument with a thermionic W source, which was operated at 100 kV. The high-resolution TEM (HRTEM) images were recorded using an image C_s-corrected JEOL JEM-2200FS TEM with a Schottky emitter, operating at 200 kV. Energy dispersive X-ray spectroscopy (EDS) analyses were carried out in high-angle annular dark field-scanning TEM (HAADF-STEM) mode using the same microscope, equipped with a Bruker Quantax 400 STEM system and a XFlash 5060 silicon-drift detector (SDD, 60 mm^2 active area). For EDS analyses, non-Cu grids and an analytical holder with a Be cup were used. The reported EDS maps were obtained by integrating the Au Lα, Cu Kα, Fe Kα and O Kα peaks in the spectra. HAADF-STEM images and tilt series of the calcined catalysts were acquired using a FEI Tecnai G2 F20 instrument with a Schottky emitter operating at an acceleration voltage of 200 kV.

2.5.2. Elemental Analysis

The chemical composition of the colloidal NCs as well as the metal loadings of the catalysts were measured by Inductively Coupled Plasma-Optical Emission Spectroscopy (ICP-OES) using an iCAP 6000 Thermo Scientific spectrometer. A specific weight (in the case of powder catalysts) or volume (in the case of colloidal solutions) was digested in HCl/HNO_3 3:1 (v/v) overnight, diluted with deionized water (14 µS) and filtered using PTFE filter before measurement.

2.5.3. X-Ray Diffraction (XRD)

XRD patterns were recorded on a Rigaku SmartLab X-Ray diffractometer equipped with a 9 kW Cu Kα rotating anode (operating at 40 kV and 150 mA) and D\teX Ultra 1D detector set in X-ray reduction

mode. The diffraction patterns were collected at room temperature by Bragg-Brentano geometry over an angular range: 2θ = 20°–85°, with a step size of 0.02° and a scan speed of 0.2 °/min. Initially, fresh NCs were deposited on a zero diffraction silicon wafer which was placed in a furnace and exposed to a heat treatment in an air atmosphere for 10 h at 350 °C (heating rate of 5 °C/min). The XRD patterns were then collected in this way from the calcined non-supported NCs. XRD data analysis was carried out using PDXL 2.7.2.0 software from Rigaku.

2.5.4. X-Ray Absorption Fine Structure Spectroscopy (XAFS)

Measurements were performed at the XAFS beamline at the Elettra synchrotron light source [24] in Trieste, Italy. The activated catalysts were diluted with polyvinylpyrrolidone (PVP) powder and pressed into pellets. Next, the pellets were mounted column-wise in a special motorized sample holder which allowed for selecting a desired sample without opening the sample chamber. The X-ray absorption near edge structure (XANES) and the extended X-ray absorption fine structure (EXAFS) spectra were collected at the Fe K-edge (7112 eV), Cu K-edge (8979 eV) and Au L_3-edge (11919 eV) in transmission mode with ion chambers detectors. The spectra of references, i.e. Fe_3O_4 (magnetite), γ-Fe_2O_3 (maghemite), α-Fe_2O_3 (hematite), $CuFe_2O_4$ (cuprospinel), Fe foil, Cu and Au foils, were collected for comparison and signal calibration. The collected data were normalized using the Athena code within the Demeter package (version 0.9.25) [25]. The EXAFS part of the spectra was obtained by converting the normalized data from energy space to k space and weighted by k^2, then Fourier transformed in the selected k range using a Hanning window. The fitting of the data was then accomplished having considered the selected models using the Artemis code within the same Demeter package. Details of the modeling are given in the supporting information (SI).

2.5.5. X-ray Photoelectron Spectroscopy (XPS)

XPS was performed on the activated catalysts using a Kratos Axis Ultra DLD spectrometer equipped with a monochromatic Al Kα source (15 kV, 20 mA). High resolution narrow scans were performed at a constant pass energy of 10 eV and steps of 0.1 eV. The photoelectrons were detected at a take-off angle Φ = 0° with respect to the surface normal. The pressure in the analysis chamber was maintained below 7×10^{-9} Torr for data acquisition. The data were converted to VAMAS format and processed using CasaXPS software, version 2.3.16. The binding energy (BE) scale was internally referenced to the C 1s peak (BE for C-C = 284.8 eV).

2.5.6. In-situ Diffuse Reflectance Infrared Fourier Transform Spectroscopy (DRIFTS)

Spectra were collected on the activated catalysts that were unloaded after the reaction test. A Vertex 70 infrared spectrometer (Brüker Optics) equipped with a DRIFTS cell (Praying Mantis, Harrick) and a Mercury Cadmium Telluride detector (MCT) cooled with liquid nitrogen was used to this purpose. The outlet of the DRIFTS cell was connected to an on-line mass spectrometer (Pfeiffer Vacuum Omnistar GSD 320). Using a 4 port selector valve, the inlet gas was switched between two different gas streams, one for purging and/or pretreatments (6% v/v O_2 and balance He) and the other containing the probe gas (0.25% v/v CO and balance He), both with a flowrate of 80 Ncc/min. The loaded sample was pretreated prior to the measurements at 350 ºC for 1 h (at a heating rate of 20 ºC/min), after which the cell was cooled down to room temperature at the same rate. Once the temperature and the signal became stable, the background spectrum was collected in the same atmosphere. Then, the sample was exposed to the probe gas and the spectra were collected every 10 s for the first 100 s of adsorption. The adsorption was monitored for a further 35 min, by collecting a spectrum every 5 min. The samples were subsequently purged after the measurement for 40 min while the spectra were monitored every 5 min.

2.5.7. Temperature Programmed Reduction using CO (CO-TPR)

The CO-TPR measurement was performed using a micro-reactor system coupled with an NDIR analyzer (ABB Uras 26) to monitor the CO and CO_2 outlet concentrations. In this regard, 15 mg of the samples were diluted with 65 mg of alumina and loaded into a micro-reactor. Next, the samples were pretreated at 350 °C for 3 h in an oxidizing atmosphere of 6% v/v O_2 balanced with He and a flow rate of 40 Ncc/min. After cooling down to room temperature, the mixture was changed to 1% v/v CO balanced with He and the system was left to fully stabilize. Then, the temperature was raised to 750 °C at a heating ramp of 15 °C/min and kept there for 1 h.

2.5.8. DFT Calculations

The calculations were based on the Density Functional Theory (DFT) as implemented in the PWsuite of the open source Quantum Espresso package [26]. The plane waves basis set was limited by the energy cutoff of 40 Ry. The electron density cutoff was set to 420 Ry. The interaction between the valence electrons and the ions for Fe, O, and Cu was described by ultrasoft pseudopotentials, with a Perdew, Burke and Ernzerhof functional. The structural and electronic properties of bulk Fe, FeO, and Cu were in good agreement with other results reported in literature. In order to correctly describe the

interactions among the d-Fe electrons we used the DFT + U approach. The value of the U parameter was set to 4 eV, which is in agreement with the values reported in literature. All the calculations were spin-polarized. A mesh grid (4 × 4 ×1) was chosen to sample the Brillouin Zone, with a Marzari-Vanderbilt [27] smearing of 0.002 Ry. The surface was modeled through the slab method (17 atomic layers) and the external surfaces were separated by 21.2 Å of vacuum. The calculations were dipole corrected. The atomic positions were optimized using the Broyden, Fletcher, Goldfarb, and Shanno (BFGS) algorithm until the forces on the atoms were less than 0.01 eV $Å^{-1}$.

3. Results and Discussion

3.1. Catalysts preparation

Our group recently reported the synthesis of dumbbell-like AuCu/FeOx NCs and their characterization with several techniques [20]. In addition, we have shown that these NCs transform upon activation to a nanocomposite with Au in the M domain and a Cu-poor cuprospinel phase in the MOx domain, while the dumbbell morphology was preserved. In this work, we manipulated the synthesis conditions using the same AuCu seeds in order to obtain nanostructures with different properties in the MOx domain. By lowering the amount of OlAc in the synthesis, we were able to adjust the oxidation extent of Fe in the MOx domain which, in turn, resulted in an increase in the population of NCs characterized by a Fe-rich core in the MOx domain. Figure S1 displays the TEM images of as-synthesized NCs along with the size distributions of both the M and MOx domains in insets. The mean size of the M domain and the external diameter of the MOx ones in the samples were estimated by statistical analysis on the TEM images, which showed comparable values of ~5.7 nm for the M domain and ~15.7 nm for the MOx (see Table S1). To characterize the observed core-shell structure of the MOx domains, one typical NC with such morphology was analyzed by STEM-EDS. As shown in Figure S2, the elemental mapping of a NC highlighted that the core of the MOx domain was richer in Fe. Considering the proportional relationship between the EDS signal intensity to the atomic density, and the decrease of Fe density with the increase of its oxidation state in oxides, we concluded that the Fe-rich core is less oxidized than the shell. This is in line with the literature on the effect of OlAc in the synthesis of Fe NPs [28]. It is noteworthy that the samples had the same (Au+Cu)/Fe and Au:Cu molar ratios, as proven by ICP analysis (see Table S1).

The as-prepared NCs were further deposited on the γ-alumina according to the procedure discussed in the Experimental section and calcined to remove the protecting ligands and activate the M domains. The elemental loadings of the catalysts were comparable, as measured by ICP-OES (see Table 1).

The activated catalysts were examined by electron microscopy and representative HAADF-STEM images of the samples are shown in Figure 1. The activation pretreatment was the harshest set of conditions to which the catalysts were exposed and therefore the stability of the catalysts during the activity measurements was ascertained. Apart from a good dispersion of the metal domains on the support (the brighter particles in the HAADF-STEM images), the formation of dumbbell NCs with a hollow MOx domain was clearly observed, particularly for the D2-A and D3-A samples. In addition, several tilted NCs were found in all three samples, with their 2D projections clearly showing a dumbbell rather than a core-shell morphology. As in the case of the NCs with full MOx domains [20], the series of tilted HAADF-STEM images on the D3-A sample further indicated that the dumbbell morphology was mostly preserved in the case of NCs with a hollow MOx domain (see Movie IS1 and the extracted images from the tilted series in Figure S3). The population of NCs with a hollow MOx domain, though not statistically measured, increased from D1-A to D3-A, which is in line with the increase in NCs having a Fe-rich core in the as-synthesized NCs. This suggested that the hollow oxide NCs were formed by the oxidation of Fe in those NCs with Fe-rich cores, most likely by a mechanism known as the Kirkendall effect, as is thoroughly explained for a number of NPs [29-33]. While the mean sizes of the M and MOx domains were found to be similar across the samples (see insets in Figure 1), a small decrease was found in the size of the M domain compared to that of the fresh NCs, which is likely due to the dealloying of Cu upon activation [20]. According to elemental mapping of a NC with a hollow MOx domain (obtained by STEM-EDS), the Au was localized in the M domain whereas the Fe and Cu were distributed in the MOx domain (see Figure S4), which is similar to our previous observation for NCs with a full MOx domain [20]. The decrease in the size of the M domain is in line with the transformation of AuCu domains to Au in the activated NCs (see SI for details of calculation). Eventually, a HRTEM of a NC with a hollow MOx domain revealed that small patches of maghemite and hematite could be observed in the largely disordered MOx domain (see Figure S5). On the other hand, NCs with a full MOx domain were found to be composed of Au and maghemite with Cu incorporated into the MOx [20].

The surface species on the activated catalysts were probed by XPS and CO-DRIFT. The former revealed a similar situation in all three samples i.e. Au^0 in the M domain and fully oxidized Fe species (Fe^{3+}) in the MOx domains excluding the presence of Fe^{2+} (see Figure S5 in the SI for a more detailed discussion).

CO adsorption was studied by DRIFT spectroscopy (Figure 2). By this technique, it is possible to identify a slight change in the surface charge, especially for Au-based catalysts [23,34,35]. All three samples showed the formation of a main carbonyl band at the wavenumber of ~2121 cm^{-1} during 35 min of gas exposure, which is assigned to the Au^0 species [23,35]. A shoulder-like feature was present at 2142 cm^{-1} for D1-A, causing the peak to be slightly asymmetrical. This feature, which is assigned to more positively charged Au species [23,35], diminished in D2-A and D3-A. In order to differentiate between these two peaks, the absorption spectrum of the samples at 35 min was deconvoluted considering a Gaussian function (see Figure S7). It was found that the contribution of the shoulder feature decreased from ~26% of the total area of the absorption band for the D1-A to ~10% for D2-A and finally it disappeared for D3-A which could be a semi-quantitative indication of the presence of different MSIs. The presence of Cu^+, which can be formed due to reduction of Cu^{2+} species when exposed to CO [36] was investigated. Such a reduction would result in the formation of carbonyl band in the range 2110-2160 cm^{-1}, accompanied to the formation of carbonates [36]. We first checked the spectra in the carbonate region. As shown in Figure S8, no specific difference was observed in the vibration frequencies of the main carbonate features [37] between the D1-A, D2-A, D3-A samples and the alumina support, while the intensities were different considering the higher oxidation activity of the samples compared to alumina. In addition, we compared our catalysts with a Au-Iron oxide catalyst, i.e. without Cu present, previously reported by us [22] and observed the same main features in the carbonate region. Although the assignment in this region is not very straightforward because of several possible carbonate structures [37], the results indicated no information on the possible contribution of Cu oxide species. Thus, we monitored the spectra in the carbonyl region during 40 min of desorption. As shown in Figure S9, the carbonyl band completely disappeared in all samples. This essentially ruled out the possibility of the presence of Cu^+ surface species as they can form stable carbonyls that are resistant to evacuation [23,38]. The carbonyls on Cu^{2+} sites could be discarded as well since their unlikely formation with a band around 2200 cm^{-1} is only reported at low temperature or high CO equilibrium pressure [38,39]. The presence of Cu^0 species was not considered with respect to the oxidizing nature of the high-temperature pretreatment performed on the samples before the DRIFT

experiment. Noteworthy to mention that no carbonyls can be formed on Fe^{3+} as well due to a the covalency of the Fe-O bond and/or saturation of coordination [40].

Catalytic activity results

The catalytic properties of the particles were systematically studied in a CO oxidation reaction through kinetic measurements and the results are shown in Figure 3, in which the rates are normalized based on the Au loading measured by ICP. Indeed, an interesting trend was observed in the kinetic tests: the D1 sample, i.e. the sample with the lowest population of dumbbell NCs with hollow oxide domains, exhibited the highest CO oxidation rate while the activity progressively decreased by increasing the population of NCs with hollow MOx domains in D2 and D3. It should be noted that the activation energy (E_a) was estimated using the Arrhenius equation and was found to be similar for all the samples, being in the order of 40 kJ/mol suggesting that the rate limiting step of the reaction was the same among the tested samples. In addition, considering more than 3.5 fold increase of the activity from D3 to D1 and the fact that the size of the MOx domain is the same among the samples, we can reasonably claim that the activity was not coming from the MOx domains. In this case indeed, a 3.5 fold decrease of the MOx diameter, resulting in a corresponding increase of the specific surface area should have been observed in order to account for the increase of activity.

3.2. Structural properties

The crystalline structures of the NCs were initially investigated by XRD. As shown in Figure 4, all calcined NCs had similar patterns, indicating the presence of Au and maghemite upon calcination, which is in line with our previous report [20]. For the D3-A sample, a contribution was also observed from a hematite phase, as the HRTEM results suggested. The standardless whole pattern fitting analysis method, known as the Fundamental Parameter (FP) method (implemented in PDXL 2.7.2.0 software), was used to determine the crystallite size (assuming an ellipsoidal crystallite shape model). The estimated values are summarized in Table 2 along with the ratio of the present phases that was obtained by semi-quantitative analysis based on the Reference Intensity Ratio (RIR). First, it was observed that the crystallite sizes of the Au and maghemite domains were quite similar in all samples, which is in line with the mean sizes of M and MOx domains that were obtained by TEM analysis. However, their contributions to the diffraction patterns were different based on the RIR and, indeed, the ratio of gold to maghemite increased from D1-A to D3-A. This could also be visually inferred from the XRD patterns, as they were normalized based on the 100% peak of Au. The phase quantitation results were further

used to obtain the Au/Fe elemental ratio in the samples which gave 0.45, 0.56 and 0.69 for D1-A, D2-A and D3-A, respectively. Interestingly, the actual value for all three samples obtained by ICP, i.e. 0.24, was close to the D1-A sample. This confirmed that the nature of oxide in the case of the hollow MOx domains was more disordered than in the full MOx ones and eventually it was not detectable by means of X-rays diffraction.

XAFS spectroscopy was applied to study the structural properties of the activated catalysts. The spectra were collected at different absorption edges, namely at the Au L_3-edge (11919 eV), Cu K-edge (8979 eV) and Fe K-edge (7112 eV), which correspond to the elements that are present in our system. The XANES spectra of the activated catalysts at different edges are compared in Figure S10. Looking at the data relating to the Au L_3-edge (Figure S10-a), it was evident that the samples had similar absorptions profiles, without having a shift in the absorption edge, which suggests that all the Au samples had the same oxidation state. All samples resembled the XANES spectrum of metallic Au, which is featured by a dampening of the white line intensity at the energy ~11925 eV [20,41]. Comparing the XANES spectra of the samples at the Cu K-edge (Figure S10-b) also revealed that the Cu in the activated catalysts have the same oxidation state while a difference was observed in the intensity of the white line, possibly due to the variation in the average coordination number from D1-A to D3-A. Moreover, the absence of sharp features below 8990 eV indicated that Cu^{2+} ions are coordinated in a more centrosymmetric configuration (such as octahedral sites) than in the bulk reference (i.e. CuO). The XANES spectra of the activated samples at the Fe K-edge (Figure S10-c) proved a similar oxidation state for Fe in all samples with the spectra resembling that of maghemite [20]. A small difference was observed in the intensity of the white line in the case of the Cu-K edge, suggesting a difference in the average coordination number of the Fe absorbers, which possibly resulted from the increase in NCs with a hollow MOx domain, and the consequent decrease in the long-range order. All samples also featured a pre-edge peak at an energy of ~7114 eV which could be attributed to the 1s to 3d transition, suggesting the existence of some non-centrosymmetric absorption sites such as tetrahedral positions [42,43] which is expected in a maghemite crystalline structure.

Moreover, the absorption spectra were further converted into the k space and the EXAFS functions were extracted from the post edge region (see Figure S11). The k^2-weighted EXAFS functions were then Fourier transformed to isolate the contribution of different scatterings from neighboring atoms as a function of radial distance (see Figure 5). The k^2-weighted EXAFS functions of the activated samples

at the Au L_3-edge and the magnitude of their Fourier transforms (|FT|) are shown in Figure S11-a and Figure 5-a, respectively. The EXAFS functions and |FT| were identical for all the samples, which is in line with the XANES results, suggesting the formation of the Au phase after activation. The peaks in Figure 5-a could be attributed to different Au-Au shells around the Au absorbers, as is confirmed by simulation (see Figure S12 and Table S2).

The EXAFS functions of the activated samples at the Cu K-edge (Figure S11-b) indicated the same pattern across the samples, i.e. the oscillations occur at the same k, while the amplitudes decreased from D1-A to D3-A. This could be attributed to a more disordered nature of the sample [44] or the decrease in the average coordination number due to the termination effect in NCs with a smaller size [45,46], both of which are consistent with the formation of hollow MOx domains, resulting in a decrease in the crystallinity. On the other hand, Figure 5-b showed the presence of a shell in the |FT| for all activated samples at a low radial distance, which is typical of metal-O shells, while two more shells with different intensities in the form of a main peak with a clear shoulder could be observed at higher radial distances. In principle, these two shells can be attributed to the presence of metal cations at octahedral and tetrahedral positions of a cubic oxide with a spinel-like structure [44]. Since we have proven the formation of Cu^{2+} upon activation as well as its possible incorporation into the octahedral vacancies of the resulted oxide domain [20], we assumed the presence of a spinel-like structure, i.e. maghemite, in which the octahedral cation vacancies are partially filled with Cu atoms. Indeed, the results of the simulation highlighted the increase in the termination effect from D1-A to D3-A, as the average coordination numbers of each shell around the Cu absorbers, specifically for the higher shells, was decreasing at a constant σ^2 (see Table S3). This indicates an increase in disorder and a decrease in nanostructure size in the case of the hollow MOx domains, which is in line with XRD results.

EXAFS functions of the activated samples at the Fe K-edge (Figure S11-c)also showed a similar trend to that of the Cu K-edge, i.e. the amplitude of oscillation decreased from D1-A to D3-A. This again suggested on the one hand a similarity in the crystalline structure of the samples, and on the other hand the increased disorder - or rather the termination effect due to further reducing the size of the nano MOx domains - in the case of a higher population of NCs with hollow oxide. Also in this case, the |FT| revealed a typical profile for the oxides that contained both octahedral and tetrahedral positions, as shown in Figure 5-c. The simulation in this case was done considering a maghemite model in which Cu ions are incorporated into octahedral vacancies. Indeed, we observed that while most of the fitting

parameters were similar across the samples, the σ^2 factor increased from 0.011 to 0.015 for D1-A to D3-A, which is in line with the increase in disorder (see Table S4). It is noteworthy that a slight deviation was observed for the half path lengths in the higher shells of metal and oxygen in comparison with the model. This could be another indication of the incorporation of the Cu^{2+} into the maghemite structure, which can cause a minor distortion in the structure of the maghemite [47].

3.3. Reducibility of the nanosized supports

Eventually, the reducibility of the nanosized MOx domains was evaluated by means of CO-TPR. The reducibility could potentially affect the activity of the catalysts considering the fact that the CO oxidation could follow the Mars Van Krevelen mechanism [7], as is suggested for Au-iron oxide catalysts [48-50]. Indeed, in the case of Au/iron oxide catalysts, Au can cause a decrease in the strength of the Fe–O bonds in the vicinity of the Au atoms which would lead to a higher lattice oxygen mobility and subsequent enhancement in the reducibility of the iron oxide [51,52]. As shown in Figure 6, all catalysts demonstrated a similar TPR profile, while the first main peak of the reduction was shifted to higher temperatures from D1-A to D3-A. The profile resembled a CO-TPR of the Au-iron oxide system that was reported by Pires et al. [47]. The incorporation of Cu – or rather, the amount of Cu loadings in our samples - did not have a significant effect. In addition, no distinct peak could be observed for the reduction of Cu, possibly due to its low loading, with the pattern being dominated by the Fe reduction signal. Nevertheless, when the MOx domains were hollow, the reduction of the Fe, which could be facilitated by the attachment of Au (as already shown in [22]), was indeed hindered, which is probably due to the reduced interface that was in contact with Au and possibly due to a different strain on the oxide. Alternatively, it can also be related to the disordered nature of the oxide in the case of hollow MOx as it has been shown to be responsible for lowering the reducibility in other oxide based materials [53]. Any of the above-mentioned reasons is undoubtedly indicative of an alteration in the MSI.

To cross check these issues and to study the possibility of removing O from the oxide domain, we performed DFT calculations on a number of models characterized by an oxygen terminated facet (001) of non-doped and Cu-doped maghemite (see SI for details). First, the energy required for the formation of an O vacancy from the (001) facet of the maghemite structure was calculated at different sites, namely an O atom (a) near an octahedral cation vacancy and bound to two octahedral Fe atoms, (b) near the Fe vacancy and bound to both octahedral and tetrahedral Fe atoms, and (c) far away from the octahedral vacancy and bound to two octahedral sites. Additionally, the significance of Cu

incorporation on energy for O removal in each case was studied by substituting the nearest octahedral Fe with a Cu atom. As shown in Table 3, the presence of Cu facilitates the formation of the O vacancy in all cases, most significantly when the vacancy is created near an octahedral Fe vacancy. A similar effect of Cu incorporation on the reducibility and subsequent enhancement of the O mobility has also been reported in the literature [47,54,55]. As the Cu content and its incorporation in the MOx domain was similar in the samples, the results of the calculations show that the different reducibility across the samples could be attributed to the presence of the octahedral Fe vacancies in the maghemite phase, a structural motif that is missing in the hematite phase. The DFT results show how the Fe octahedral vacancies at the surface favor the formation of the O vacancy by itself (the oxygen is more weakly bonded near the Fe vacancy, see Table 3) or as a conduit for Cu incorporation (which also favors the O vacancy formation). The presence of hematite, mostly in the D3 sample, could therefore decrease the supply of favorable sites for the MOx reduction [47].

Conclusions

To summarize, we prepared a set of Au based catalysts from colloidal dumbbell-like nanostructures which had different populations of NCs with a hollow oxide domain while maintaining a constant Au domain size. The samples showed a decrease in CO oxidation activity by increasing the number of NCs with a hollow oxide domain. We studied the relationship between the difference in the activity and the differences in the structural properties of the NCs. CO-DRIFT studies highlighted a different charge transfer when going from full to hollow oxide domains, which resulted in the decreased presence of positively charged Au species with an increase in the fraction of the hollow oxide domain highlighting the alteration of the MSI. On the other hand, XRD and XAFS results revealed that the oxide domain became more disordered as the population of NCs with a hollow oxide domain increased, and a small fraction of hematite phase appeared besides the dominant, Cu-doped, maghemite phase. It was observed that the reducibility of the nanosized oxide support was different among the samples i.e. the Fe oxide reduction was shifted to a higher temperature as the population of NCs with hollow oxide domains increased. In this regard, DFT calculations showed that the different reducibility across the samples could be attributed to the presence of the octahedral Fe vacancies in the maghemite phase, a structural motif that is missing in the hematite phase. Furthermore, the incorporation of Cu, which occurred in the case of maghemite but not in the case of hematite, could also facilitate the removal of O from its neighborhood. This could, in turn, hinder the provision of O from the nanosized support. Having the same size of the MOx domain also revealed that the MOx was not the major factor for the

enhancement of the activity from hollow to full MOx, hence the role of the Cu in the observed different activities could be ruled out. However, despite all these structural changes, the similarity of the activation energy for all samples indicated that the rate limiting step was not affected and therefore, the lower activity in case of hollow particles might be reasonably correlated with the lower number of active sites, i.e. the metal/oxide interfacial sites, likely induced by the different oxide morphology. This is not an obvious result considering the documented structural differences among the samples. For this reason, this work provides a guideline for the future development of metal-metal oxide catalytic materials. Indeed, this work highlights the role of nanoscale oxide morphology with regards to the catalytic properties of metal-metal oxide based catalysts, revealing that the morphological difference only indirectly affected the catalytic activity through modifying the number of catalytically active sites. Such a role could be highlighted thanks to the fine control of catalyst properties that was achieved through colloidal synthesis methods, and is foreseen to stimulate further research in this direction.

Acknowledgment

We acknowledge Prof. Daniela Zanchet for the support provided in the analysis of the EXAFS data. Also, we acknowledge financial support from European Union through the EU-ITN network Mag(net)icFun (PITN-GA-2012−290248).

Reference

1. Hayek, K., R. Kramer, and Z. Paál, *Metal-support boundary sites in catalysis.* Applied Catalysis A: General, 1997. **162**(1): p. 1-15.
2. Fu, Q. and T. Wagner, *Interaction of nanostructured metal overlayers with oxide surfaces.* Surf. Sci. Rep., 2007. **62**(11): p. 431-498.
3. Wang, Z., H. Fu, Z. Tian, D. Han, and F. Gu, *Strong metal-support interaction in novel core-shell Au-CeO2 nanostructures induced by different pretreatment atmospheres and its influence on CO oxidation.* Nanoscale, 2016. **8**(11): p. 5865-5872.
4. Gatla, S., D. Aubert, G. Agostini, O. Mathon, S. Pascarelli, T. Lunkenbein, M.G. Willinger, and H. Kaper, *Room-Temperature CO Oxidation Catalyst: Low-Temperature Metal–Support Interaction between Platinum Nanoparticles and Nanosized Ceria.* ACS Catal., 2016. **6**(9): p. 6151-6155.
5. Singha, R.K., A. Shukla, A. Yadav, L.N. Sivakumar Konathala, and R. Bal, *Effect of metal-support interaction on activity and stability of Ni-CeO2 catalyst for partial oxidation of methane.* Appl. Catal., B, 2017. **202**: p. 473-488.
6. Ning, X., Y. Li, B. Dong, H. Wang, H. Yu, F. Peng, and Y. Yang, *Electron transfer dependent catalysis of Pt on N-doped carbon nanotubes: Effects of synthesis method on metal-support interaction.* J. Catal., 2017. **348**: p. 100-109.
7. Ruiz Puigdollers, A., P. Schlexer, S. Tosoni, and G. Pacchioni, *Increasing Oxide Reducibility: The Role of Metal/Oxide Interfaces in the Formation of Oxygen Vacancies.* ACS Catalysis, 2017. **7**(10): p. 6493-6513.
8. Liotta, L.F., *Catalytic oxidation of volatile organic compounds on supported noble metals.* Applied Catalysis B: Environmental, 2010. **100**(3-4): p. 403-412.
9. Gélin, P. and M. Primet, *Complete oxidation of methane at low temperature over noble metal based catalysts: a review.* Applied Catalysis B: Environmental, 2002. **39**(1): p. 1-37.
10. Behafarid, F. and B. Roldan Cuenya, *Towards the Understanding of Sintering Phenomena at the Nanoscale: Geometric and Environmental Effects.* Topics in Catalysis, 2013. **56**(15): p. 1542-1559.
11. Moon, S.Y., B. Naik, C.-H. Jung, K. Qadir, and J.Y. Park, *Tailoring metal–oxide interfaces of oxide-encapsulated Pt/silica hybrid nanocatalysts with enhanced thermal stability.* Catal. Today, 2016. **265**: p. 245-253.
12. Cargnello, M., V.V.T. Doan-Nguyen, T.R. Gordon, R.E. Diaz, E.A. Stach, R.J. Gorte, P. Fornasiero, and C.B. Murray, *Control of Metal Nanocrystal Size Reveals Metal-Support Interface Role for Ceria Catalysts.* Science, 2013. **341**(6147): p. 771-773.
13. Ahmadi, M., H. Mistry, and B. Roldan Cuenya, *Tailoring the Catalytic Properties of Metal Nanoparticles via Support Interactions.* The Journal of Physical Chemistry Letters, 2016. **7**(17): p. 3519-3533.
14. Klyushin, A.Y., M.T. Greiner, X. Huang, T. Lunkenbein, X. Li, O. Timpe, M. Friedrich, M. Hävecker, A. Knop-Gericke, and R. Schlögl, *Is Nanostructuring Sufficient To Get Catalytically Active Au?* ACS Catalysis, 2016. **6**(5): p. 3372-3380.
15. Bruix, A., J.A. Rodriguez, P.J. Ramírez, S.D. Senanayake, J. Evans, J.B. Park, D. Stacchiola, P. Liu, J. Hrbek, and F. Illas, *A New Type of Strong Metal–Support Interaction and the Production of H2 through the Transformation of Water on Pt/CeO2(111) and Pt/CeOx/TiO2(110) Catalysts.* J. Am. Chem. Soc., 2012. **134**(21): p. 8968-8974.
16. Venezia, A.M., V. La Parola, and L.F. Liotta, *Structural and surface properties of heterogeneous catalysts: Nature of the oxide carrier and supported particle size effects.* Catal. Today, 2017. **285**: p. 114-124.
17. Dai, Y., Y. Wang, B. Liu, and Y. Yang, *Metallic Nanocatalysis: An Accelerating Seamless Integration with Nanotechnology.* Small, 2015. **11**(3): p. 268-289.
18. Meunier, F.C., *Bridging the Gap between Surface Science and Industrial Catalysis.* ACS Nano, 2008. **2**(12): p. 2441-2444.

19. George, C., A. Genovese, A. Casu, M. Prato, M. Povia, L. Manna, and T. Montanari, *CO Oxidation on Colloidal Au0.80Pd0.20–FexOy Dumbbell Nanocrystals.* Nano Lett., 2013. **13**(2): p. 752-757.
20. Najafishirtari, S., T.M. Kokumai, S. Marras, P. Destro, M. Prato, A. Scarpellini, R. Brescia, A. Lak, T. Pellegrino, D. Zanchet, L. Manna, and M. Colombo, *Dumbbell-like Au0.5Cu0.5@Fe3O4 Nanocrystals: Synthesis, Characterization, and Catalytic Activity in CO Oxidation.* ACS Appl. Mater. Interfaces, 2016. **8**(42): p. 28624-28632.
21. Yu, H., M. Chen, P.M. Rice, S.X. Wang, R.L. White, and S. Sun, *Dumbbell-like Bifunctional Au−Fe3O4 Nanoparticles.* Nano Lett., 2005. **5**(2): p. 379-382.
22. Najafishirtari, S., P. Guardia, A. Scarpellini, M. Prato, S. Marras, L. Manna, and M. Colombo, *The effect of Au domain size on the CO oxidation catalytic activity of colloidal Au–FeOx dumbbell-like heterodimers.* Journal of Catalysis, 2016. **338**: p. 115-123.
23. Najafishirtari, S., R. Brescia, P. Guardia, S. Marras, L. Manna, and M. Colombo, *Nanoscale Transformations of Alumina-Supported AuCu Ordered Phase Nanocrystals and Their Activity in CO Oxidation.* ACS Catalysis, 2015. **5**(4): p. 2154-2163.
24. Andrea Di, C., A. Giuliana, M. Marco, P. Emiliano, N. Nicola, C. Andrea, and O. Luca, *Novel XAFS capabilities at ELETTRA synchrotron light source.* J. Phys.: Conf. Ser., 2009. **190**(1): p. 012043.
25. Ravel, B. and M. Newville, *ATHENA, ARTEMIS, HEPHAESTUS: data analysis for X-ray absorption spectroscopy using IFEFFIT.* Journal of Synchrotron Radiation, 2005. **12**(4): p. 537-541.
26. Paolo, G., B. Stefano, B. Nicola, C. Matteo, C. Roberto, C. Carlo, C. Davide, L.C. Guido, C. Matteo, D. Ismaila, C. Andrea Dal, G. Stefano de, F. Stefano, F. Guido, G. Ralph, G. Uwe, G. Christos, K. Anton, L. Michele, M.-S. Layla, M. Nicola, M. Francesco, M. Riccardo, P. Stefano, P. Alfredo, P. Lorenzo, S. Carlo, S. Sandro, S. Gabriele, P.S. Ari, S. Alexander, U. Paolo, and M.W. Renata, *QUANTUM ESPRESSO: a modular and open-source software project for quantum simulations of materials.* Journal of Physics: Condensed Matter, 2009. **21**(39): p. 395502.
27. Marzari, N., D. Vanderbilt, A. De Vita, and M.C. Payne, *Thermal Contraction and Disordering of the Al(110) Surface.* Physical Review Letters, 1999. **82**(16): p. 3296-3299.
28. Farrell, D., S.A. Majetich, and J.P. Wilcoxon, *Preparation and Characterization of Monodisperse Fe Nanoparticles.* J. Phys. Chem. B, 2003. **107**(40): p. 11022-11030.
29. Yin, Y., R.M. Rioux, C.K. Erdonmez, S. Hughes, G.A. Somorjai, and A.P. Alivisatos, *Formation of Hollow Nanocrystals Through the Nanoscale Kirkendall Effect.* Science, 2004. **304**(5671): p. 711-714.
30. Wang, W., M. Dahl, and Y. Yin, *Hollow Nanocrystals through the Nanoscale Kirkendall Effect.* Chem. Mater., 2013. **25**(8): p. 1179-1189.
31. Peng, S. and S. Sun, *Synthesis and Characterization of Monodisperse Hollow Fe3O4 Nanoparticles.* Angew. Chem. Int. Ed., 2007. **46**(22): p. 4155-4158.
32. Cabot, A., V.F. Puntes, E. Shevchenko, Y. Yin, L. Balcells, M.A. Marcus, S.M. Hughes, and A.P. Alivisatos, *Vacancy Coalescence during Oxidation of Iron Nanoparticles.* J. Am. Chem. Soc., 2007. **129**(34): p. 10358-10360.
33. Nemati, Z., H. Khurshid, J. Alonso, M.H. Phan, P. Mukherjee, and H. Srikanth, *From core/shell to hollow Fe/ γ -Fe 2 O 3 nanoparticles: evolution of the magnetic behavior.* Nanotechnology, 2015. **26**(40): p. 405705.
34. Mihaylov, M., H. Knözinger, K. Hadjiivanov, and B.C. Gates, *Characterization of the Oxidation States of Supported Gold Species by IR Spectroscopy of Adsorbed CO.* Chem. Ing. Tech., 2007. **79**(6): p. 795-806.
35. Guo, L.-W., P.-P. Du, X.-P. Fu, C. Ma, J. Zeng, R. Si, Y.-Y. Huang, C.-J. Jia, Y.-W. Zhang, and C.-H. Yan, *Contributions of distinct gold species to catalytic reactivity for carbon monoxide oxidation.* Nat. Commun., 2016. **7**: p. 13481.
36. Hadjiivanov, K.I., M.M. Kantcheva, and D.G. Klissurski, *IR study of CO adsorption on Cu-ZSM-5 and CuO/SiO2 catalysts: [sigma] and [small pi] components of the Cu+-CO bond.* Journal of the Chemical Society, Faraday Transactions, 1996. **92**(22): p. 4595-4600.

37. Föttinger, K., R. Schlögl, and G. Rupprechter, *The mechanism of carbonate formation on Pd–Al2O3catalysts.* Chem. Commun., 2008(3): p. 320-322.
38. Hadjiivanov, K. and H. Knözinger, *FTIR study of CO and NO adsorption and coadsorption on a Cu/SiO2 catalyst: Probing the oxidation state of copper.* Physical Chemistry Chemical Physics, 2001. **3**(6): p. 1132-1137.
39. Venkov, T. and K. Hadjiivanov, *FTIR study of CO interaction with Cu/TiO2.* Catalysis Communications, 2003. **4**(4): p. 209-213.
40. Ivanova, E., M. Mihaylov, K. Hadjiivanov, V. Blasin-Aubé, O. Marie, A. Plesniar, and M. Daturi, *Evidencing three distinct FeII sites in Fe–FER zeolites by using CO and NO as complementary IR probes.* Appl. Catal., B, 2010. **93**(3): p. 325-338.
41. Kuhn, M. and T.K. Sham, *Charge redistribution and electronic behavior in a series of Au-Cu alloys.* Physical Review B, 1994. **49**(3): p. 1647-1661.
42. Westre, T.E., P. Kennepohl, J.G. DeWitt, B. Hedman, K.O. Hodgson, and E.I. Solomon, *A Multiplet Analysis of Fe K-Edge 1s → 3d Pre-Edge Features of Iron Complexes.* J. Am. Chem. Soc., 1997. **119**(27): p. 6297-6314.
43. Yao, Y., Y. Hu, and R.W.J. Scott, *Watching Iron Nanoparticles Rust: An in Situ X-ray Absorption Spectroscopic Study.* J. Phys. Chem. C, 2014. **118**(38): p. 22317-22324.
44. Calvin, S., *XAFS for Everyone*. 2013: Taylor & Francis.
45. Calvin, S., M.M. Miller, R. Goswami, S.-F. Cheng, S.P. Mulvaney, L.J. Whitman, and V.G. Harris, *Determination of crystallite size in a magnetic nanocomposite using extended x-ray absorption fine structure.* J. Appl. Phys., 2003. **94**(1): p. 778-783.
46. Wang, X., M. Zhu, L.K. Koopal, W. Li, W. Xu, F. Liu, J. Zhang, Q. Liu, X. Feng, and D.L. Sparks, *Effects of crystallite size on the structure and magnetism of ferrihydrite.* Environ. Sci.: Nano, 2016. **3**(1): p. 190-202.
47. Pires, M.d.S., F.G.E. Nogueira, J.A. Torres, L.C.T. Lacerda, S. Correa, M.C. Pereira, and T.C. Ramalho, *Experimental and theoretical study on the reactivity of maghemite doped with Cu2+ in oxidation reactions: structural and thermodynamic properties towards a Fenton catalyst.* RSC Adv., 2016. **6**(84): p. 80830-80839.
48. Daniells, S.T., A.R. Overweg, M. Makkee, and J.A. Moulijn, *The mechanism of low-temperature CO oxidation with Au/Fe2O3 catalysts: a combined Mössbauer, FT-IR, and TAP reactor study.* J. Catal., 2005. **230**(1): p. 52-65.
49. Carabineiro, S.A.C., N. Bogdanchikova, P.B. Tavares, and J.L. Figueiredo, *Nanostructured iron oxide catalysts with gold for the oxidation of carbon monoxide.* RSC Adv., 2012. **2**(7): p. 2957-2965.
50. Gupta, N.M. and A.K. Tripathi, *The role of nanosized gold particles in adsorption and oxidation of carbon monoxide over Au/Fe2O3 Catalyst.* Gold Bull., 2001. **34**(4): p. 120-128.
51. Minicò, S., S. Scirè, C. Crisafulli, R. Maggiore, and S. Galvagno, *Catalytic combustion of volatile organic compounds on gold/iron oxide catalysts.* Appl. Catal., B, 2000. **28**(3–4): p. 245-251.
52. Puigdollers, A.R. and G. Pacchioni, *CO Oxidation on Au Nanoparticles Supported on ZrO2: Role of Metal/Oxide Interface and Oxide Reducibility.* ChemCatChem, 2017. **9**(6): p. 1119-1127.
53. Poyraz, A.S., W. Song, D. Kriz, C.-H. Kuo, M.S. Seraji, and S.L. Suib, *Crystalline Mesoporous K2–xMn8O16 and ε-MnO2 by Mild Transformations of Amorphous Mesoporous Manganese Oxides and Their Enhanced Redox Properties.* ACS Appl. Mater. Interfaces, 2014. **6**(14): p. 10986-10991.
54. Khan, A. and P.G. Smirniotis, *Relationship between temperature-programmed reduction profile and activity of modified ferrite-based catalysts for WGS reaction.* Journal of Molecular Catalysis A: Chemical, 2008. **280**(1-2): p. 43-51.
55. Yan, H., X.-T. Qin, Y. Yin, Y.-F. Teng, Z. Jin, and C.-J. Jia, *Promoted Cu-Fe3O4 catalysts for low-temperature water gas shift reaction: Optimization of Cu content.* Applied Catalysis B: Environmental, 2018. **226**: p. 182-193.

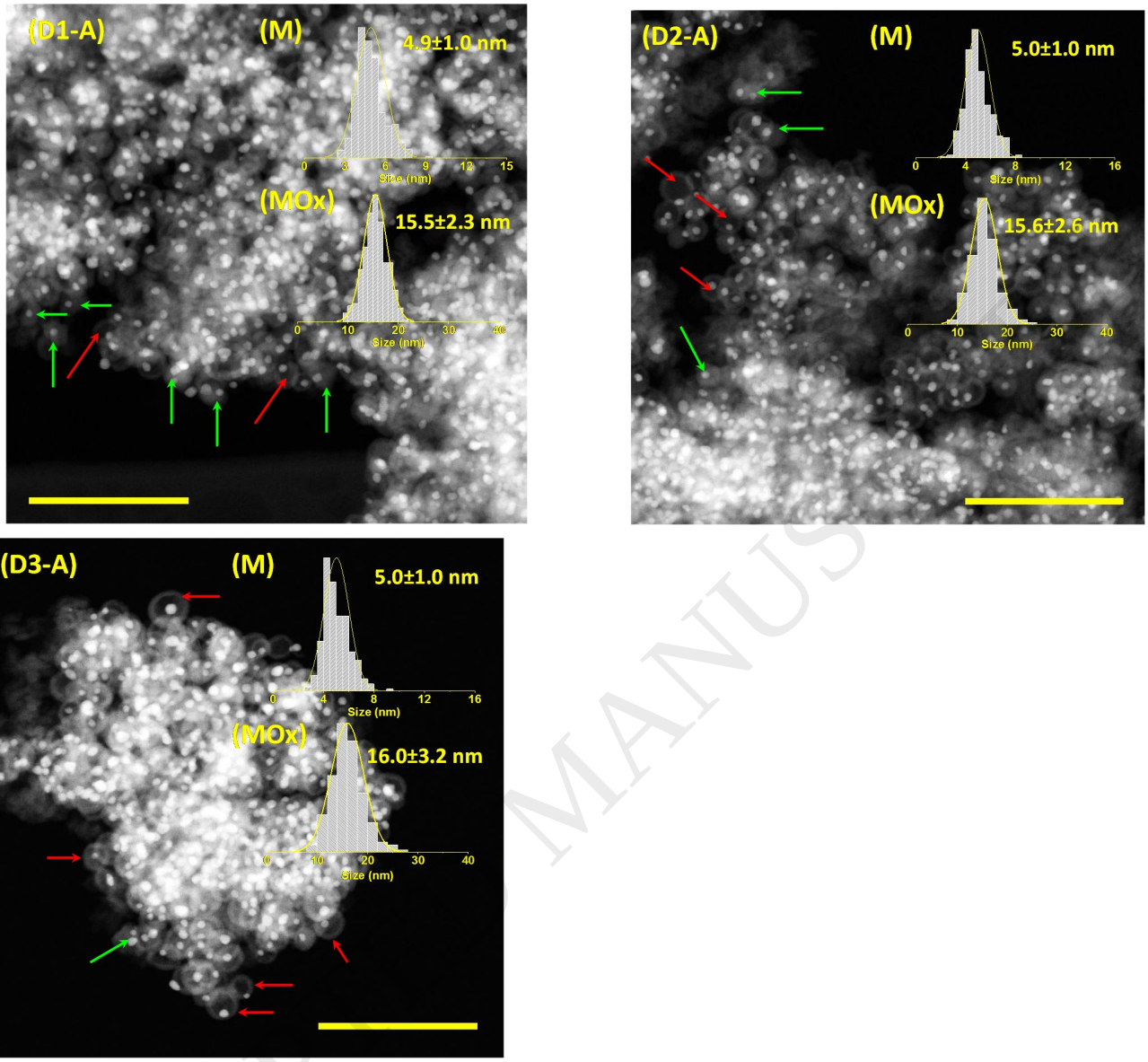

Figure 1. Typical HAADF-STEM images of the activated catalysts with the size distribution of metal (M) and metal oxide domain (MOx) as insets. The red and green arrows show the NCs with hollow and full oxide domains, respectively; the scale bars = 100 nm.

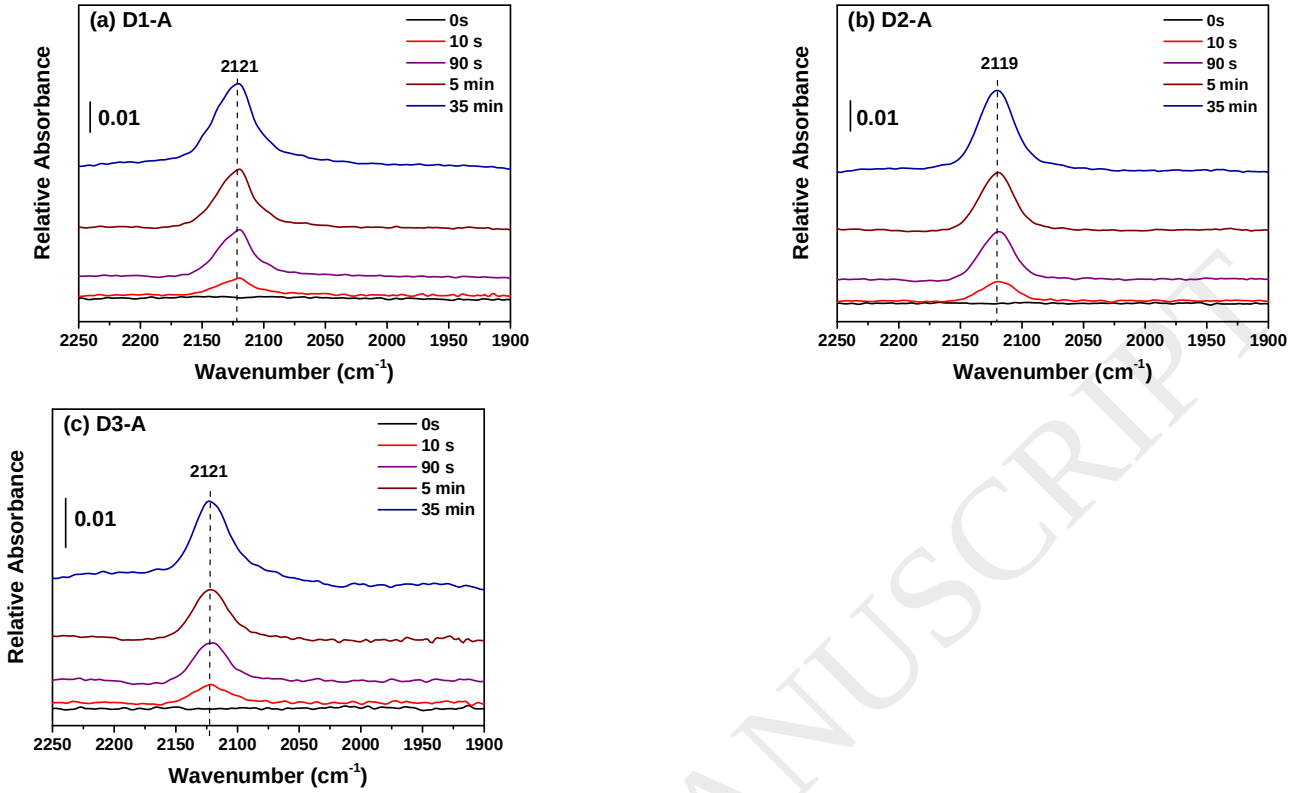

Figure 2. DRIFTS spectra in the carbonyl region, recorded during the adsorption of CO at room temperature using 0.25% v/v CO in He as a probe gas after an oxidizing pretreatment in 6% v/v O2 in He, at 350 ºC for 1 h.

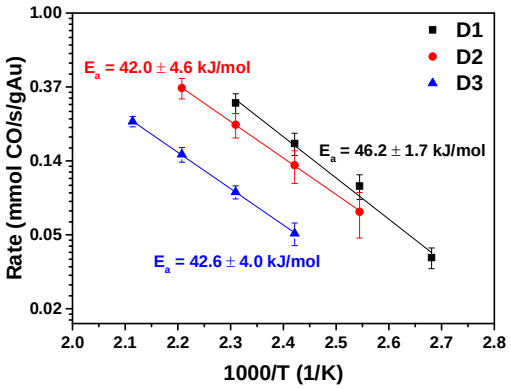

Figure 3. Kinetic data measured from the catalysts. Experimental conditions: CO = 1% v/v; O_2 = 6% v/v; WHSV= 24'000'000 Ncc/h/g(Au).

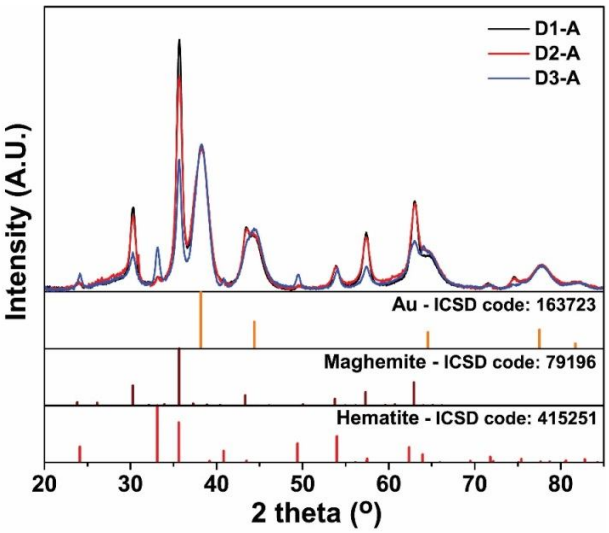

Figure 4. Comparison of the X-ray diffraction (XRD) patterns for the calcined AuCu/FeOx dumbbell NCs. Experimental data are compared with the Inorganic Crystal Structure Database (ICSD) patterns.

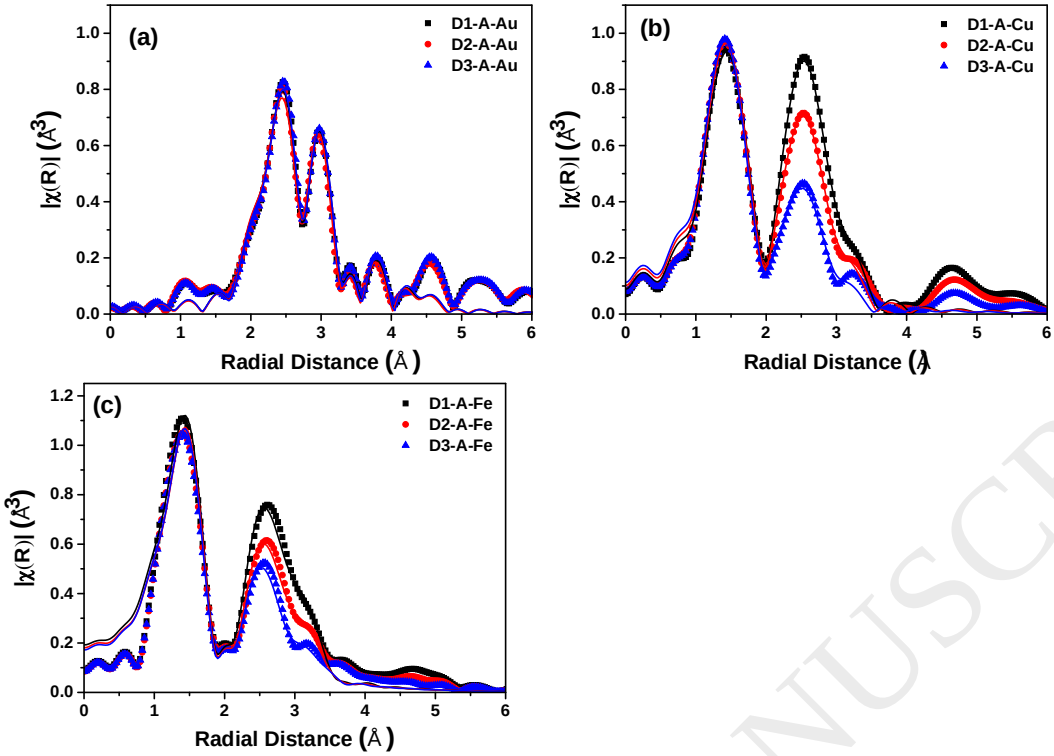

Figure 5. The magnitude of the Fourier transforms of the k^2-weighted EXAFS function for the activated catalysts at different edges of (a) Au-L_3, (b) Cu-K and (c) Fe-K. The scattered points are the experimental data while the solid lines represent the fitted profiles.

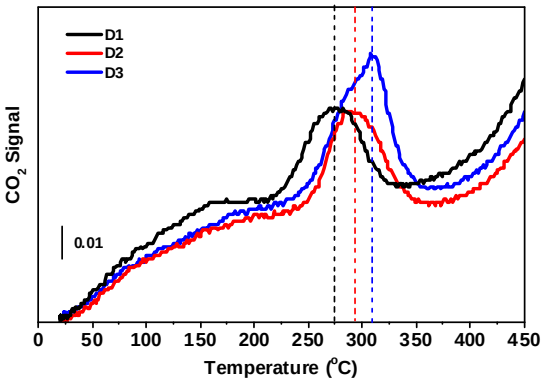

Figure 6. The comparison of CO-TPR profiles on the activated catalysts. Experimental conditions: CO = 1% v/v balance He with the flow of 40 Ncc/min.

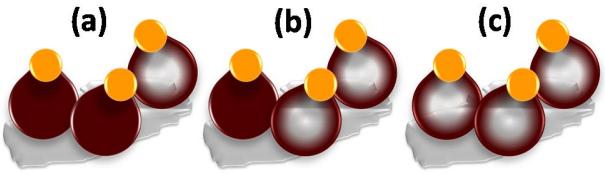

Scheme 1. The schematic illustration of different batches of activated catalysts having an increasing population of dumbbell-like NCs with oxide domain from a to c. The yellow circles represents the metal (M) domain while the brown circles represent the metal oxide (MOx) domains. The hollow oxide domains are illustrated with the same color but are more transparent (the population ratio is only schematic and does not represents the actual ratio). The gray sheet is the alumina support used as an inert carrier for the NCs.

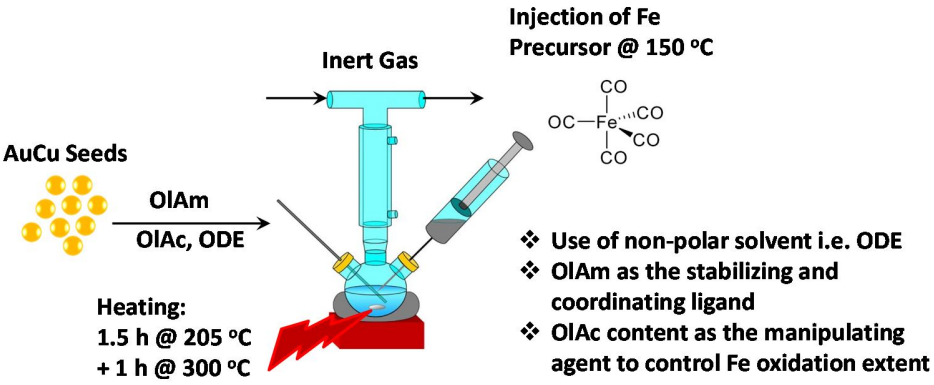

Scheme 2. A schematic illustration of the synthesis procedure that was used to prepare nanodumbbell-like heterostructures.

Table 1. Results of ICP-OES on the elemental loadings of the catalysts in terms of wt.%.

Sample Tag	Au loading (%)	Cu loading (%)	Fe loading (%)
D1-A	1.11	0.36	4.50
D2-A	0.87	0.31	3.67
D3-A	0.93	0.32	3.82

Table 2. Results of XRD analyses: crystallite sizes and phase quantification.

Sample	Crystallite Size (nm)		Phase Quantification from RIR (%)			
	Au	Maghemite	Au	Maghemite	Hematite	Au/Fe (molar)
D1-A	5.8	13.5	20.8	79.2	–	0.45
D2-A	5.7	11.7	24.1	75.9	–	0.56
D3-A*	5.3	13.2	27.5	55.4	17.1	0.69*

* for this sample, the quantification was performed considering both maghemite and hematite phases.

Table 3. Formation energy of an oxygen vacancy by the removal of an O atom: **(**a) near an octahedral cation vacancy and bound to two Fe octahedral sites, (b) near the Fe vacancy and bound to both octahedral and tetrahedral Fe atoms, and (c) far away from the octahedral vacancy and bound to two octahedral Fe sites.

Case	**$E_{formation}$ * (eV)**	
	Without Cu	**With Cu**
(a)	0.32	-0.15
(b)	1.66	1.49
(c)	2.22	1.75

* see SI for the details of calculations.